

**Convective Structures in a Simulated Torrential-Rain-Producing  
Mesoscale Convective System in East China**

Jordan Foley

A scholarly paper in partial fulfillment of the requirements for the degree of

Master of Science

May 2014

Department of Atmospheric and Oceanic Science, University of Maryland  
College Park, Maryland

Advisor: Dr. Da-Lin Zhang

## Table of Contents

<b>Abstract</b> .....	iii
<b>Acknowledgements</b> .....	iv
List of figures .....	v
List of symbols .....	ix
<b>Chapter 1 Introduction</b> .....	1
1.1 Previous Studies of Extreme Rainfall .....	2
1.2 Previous Studies of Convective Organization .....	6
1.3 Significant Findings from Part I. ....	8
1.4 Objectives of this Study .....	10
<b>Chapter 2 Model description</b> .....	13
<b>Chapter 3 Results</b> .....	15
3.1 Distribution and Evolution of Rainbands .....	15
3.2 Formation and Orientation of Rainbands .....	24
3.3 Evolution of Variable Maximums .....	30
3.4 Evolution of Rainband Vertical Structure .....	34
<b>Chapter 4 Summary and Conclusions</b> .....	43
<b>References</b> .....	47

## Abstract

A 24-h multi-nested model with smallest grid size of 444 m is used to simulate the mesoscale features of a nocturnal extreme-rainfall-producing mesoscale convective system (MCS) over East China during 3-5 July 2003. Initial model analysis indicates the presence of strong linearly oriented rainbands passing through the Chuzhou region where the torrential rainfall was recorded. Nocturnal surface instability and deep atmospheric moisture content reveal an ambient atmosphere ripe for widespread mesoscale convective development in and around the larger MCS structure.

Further analysis of the overlying atmosphere reveals a low-level directional shear oriented in a SW-NE fashion, allowing boundary layer roll vortices to form parallel to the shear direction. The rising terminus of these roll vortices thus condense to form heavily precipitating convective bands, given the high levels of atmospheric moisture present. Propagating eastward with the MCS, these rainbands exhibit band training where each band adds to the extreme rainfall total at Chuzhou. The model replications show the passage of one convective cell, eventually forming the leading convective line, to be most responsible for Chuzhou rainfall due to extreme rain rates from the evolution of relevant variable maxima (cloud hydrometeors, vertical velocity, and convergence). A breakdown of the vertical rainband structure further broadens our understanding of torrential rainfall production, as the along line vertical structure suggests echo training of convective cells within the rainband and the cross line vertical band structure illustrates the interaction of the inflow with the MCS outflow, leading to hydrometeor loading and precipitation formation.

## **Acknowledgements**

There are a few individuals I would like to graciously single out and thank for their support in the development of this paper.

First and foremost, I want to show my greatest appreciation to my advisor Dr. Da-Lin Zhang, who helped me along with this paper every step of the way. Thank you for sparking my academic mind and driving me to become a better scientist.

I would also like to thank both Man Zhang and Lin Zhu, who both contributed plotting scripts and assisted in code development for this paper. Their assistance was critical in plotting necessary features for this study.

Lastly, I want to show my deepest gratitude to my parents, Thomas and Teresa Foley. Their undying support and faith in me provided the mental and emotional support needed to complete this research paper.

## List of Figures

<u>Figure</u>		<u>Page</u>
1	<p>Horizontal distribution of flow vectors, <math>\Theta_e</math> (solid contoured at 2K intervals), and radar reflectivity (color shaded) at <math>z = 500</math> m</p> <p>From (a) 15-h; (b) 16-h; (c) 17-h; (d) 18-h; (e) 19-h; and 20-h Simulations over D4. “X” denotes the location of Chuzhou.....</p>	16
2	<p>Simulated surface reflectivity (mm shaded), 20 min rainfall (contoured, 5 mm intervals), and storm-relative surface flow vectors at (a) 1620Z; (b) 1640Z; (c) 1700Z; (d) 1720Z; (e) 1740Z; (f) 1800Z; (g) 1820Z; and (h) 1920Z. Convective cells A, B, C, D, and E denote relevant convective cells, with “X” representing the location of Chuzhou.....</p>	20
3	<p>20-min rain rate (mm) time series at the point of maximum 24 hour (00Z 4 July 2003 – 00Z 5 July 2003) rainfall accumulation (blue – 32.41°N, 118.5°E) and the point of maximum rain rate (red – 32.375°N, 118.5°E) over D4 during the 24 hour period.</p> <p>A, B, C, and D represent convective cells relevant to extreme rainfall totals.....</p>	22
4	<p>Horizontal distribution of CAPE (<math>J\ kg^{-1}</math>, shaded), vertical motion</p>	

( $\text{m s}^{-1}$ , solid/upward, dashed/downward), and flow vectors at  $z =$   
1 km for (a) 16-h; (b) 18-h; and (c) 20-h. CAPE maximized at  
966 mb. Heavy dashed line represents leading edge of 40+ dBZ..... 24

5 (a) Area average hodograph ( $\text{m s}^{-1}$ ) in the lowest 400 mb at 16-h  
(b) 16-h 1 km vertical motion ( $\text{mm s}^{-1}$ ). Solid black line represents  
leading convective edge at 20+ dBZ. The square box within represents  
the area average for (a), while the west-east cross section is shown in  
(c). (c) Vertical cross section of vertical motion (shaded  $\text{mm s}^{-1}$ ) and  
 $\Theta$  perturbations (contoured at 0.2 K) taken normal to the shear vector  
in the lowest 3-5 km of the pre-storm environment from the 16-h  
simulation over subdomain D4..... 26

6 Area averaged skew-T/log-P diagrams taken (a) ahead of; (b) at the  
leading convective line (location of peak updraft/reflectivity); and  
(c) in the trailing stratiform region of the MCS from the 17-h simulation.  
Soundings are averaged over 5 equidistant points within each indicated  
region at the top left reflectivity map..... 29

7 Time series of (a) the peak updraft  $\text{m s}^{-1}$ , green, y-axis on left) and the  
peak convergence ( $\text{s}^{-1}$ , red, y-axis on right); and (b) the peak cloud  
hydrometeors ( $\text{g kg}^{-1}$ , blue, y-axis on left) and the peak integrated

	hydrometeors (cm, purple, y-axis on right). Each time series covers 13 – 20-h over D4 simulation.....	31
8	Vertical profiles of maximum (a) vertical motion; and (b) cloud hydrometeors at each color coded time over D4 simulation. X-axis denotes variable value, whereas y-axis denotes isobaric height (mb).....	33
9	Along line cross-sections of simulated reflectivity (dBZ shaded), cloud hydrometeors (2.0 g kg <sup>-1</sup> black contour intervals), $\Theta_e$ (3 K grey contour intervals), and temperature perturbations (1 K purple dashed contour intervals) superimposed with in-plane flow vectors at (a) 1640Z; and (b) 1720Z. Plan view maps on left indicate cross-section locations, with “X” denoting the location of Chuzhou.....	35
10	Normal cross-sections of simulated reflectivity (dBZ shaded), cloud hydrometeors (2.0 g kg <sup>-1</sup> black contour intervals), $\Theta_e$ (3 K grey contour intervals), and temperature perturbations (1 K purple dashed contour intervals), superimposed with in-plane flow vectors at (a) 1620Z; and (b) 1640Z. Plan view maps on left indicate cross-section locations, with “X” denoting the location of Chuzhou.....	38

11	<p>Normal cross-sections of simulated reflectivity (dBZ shaded), cloud hydrometeors (<math>2.0 \text{ g kg}^{-1}</math> black contour intervals), <math>\Theta_e</math> (3 K grey contour intervals), and temperature perturbations (1 K purple dashed contour intervals) superimposed with in-plane flow vectors at (a) 1720Z; and (b) 1740Z. Plan view maps on left indicate cross-section locations, with “X” denoting the location of Chuzhou.....</p>	39
12	<p>Simulated reflectivity (dBZ shaded), cloud hydrometeors (<math>2.0 \text{ g kg}^{-1}</math> black contour intervals), and 20 min rainfall (10 mm grey dashed contour intervals) at 20-h simulation. Heavy black lines indicate locations of cross-sections for Fig. 13.....</p>	40
13	<p>Normal cross-sections of simulated reflectivity (dBZ shaded), cloud hydrometeors (<math>2.0 \text{ g kg}^{-1}</math> black contour intervals), and <math>\Theta_e</math> (3 K grey contour intervals), superimposed with in-plane flow vectors at 20-h simulation. Thick black line represents freezing level (<math>0^\circ\text{C}</math>).....</p>	41

## List of Symbols

- $\Theta$  Potential Temperature
- $\Theta_e$  Equivalent Potential Temperature

## Chapter 1. Introduction

Mesoscale convective systems (MCSs) are organized clusters of convective cells that are often associated with severe weather phenomena, most notably extreme rainfall production resulting in flash flooding. A large conglomeration of convective activity typically qualifies as an MCS when the precipitating region extends 100 km or greater in some direction horizontally (Houze 2004) and to the top of the troposphere vertically, the latter of which is a defining characteristic of any heavily precipitating cumulonimbus cloud. During the summer in East China, from May to July, these MCSs form along the Meiyu front, a quasi-stationary front providing the atmospheric ingredients necessary (surface heating and instability, abundant water vapor content, and low-level ambient wind shear) for initiating widespread, organized convective storms (Ding 1994).

MCS structure is most commonly observed and defined by strong squall-line convective activity along the leading outflow boundary, complimented by a larger trailing stratiform region behind. However, this is not the only possibility, as more uncommon MCS formations have also been observed where the stratiform region instead precedes the heaviest convective development (Parker and Johnson 2004, Parker 2007). Nevertheless, the opportunity for extreme rainfall production given these structural options would only affect the timing of the heaviest precipitation, not the overall precipitation totals.

Within the larger MCS structure, more localized convective structures materialize and propagate as part of the larger MCS system, resulting in sizeable rainfall accumulations during passage as consecutive storm cells within a rainband

pass repeatedly over the same locations with time. This phenomenon, known as echo training, is known to cause flash flooding by producing extreme rainfall totals over the affected regions (Doswell et al. 1996; Houze et al. 1990; Schumacher and Johnson 2005). The synoptic and mesoscale features of an MCS which result in heavy precipitation production, such as the aforementioned echo training, have been modeled at several kilometers at best (Kain et al. 2008; Lean et al. 2008), resulting in an understanding of the locations of heavy convective rainfall as well as the synoptic scale environmental characteristics governing development of the mesoscale MCS features, including the leading convective boundary, stratiform region, and echo-trained convective precipitation bands.

## **1.1 Previous Studies of Extreme Rainfall**

A large fraction of mid-latitude extreme-rainfall-producing events may be attributed to some variation of an MCS. Due to their large lateral extent and relatively slow propagation, MCSs have the potential to precipitate several inches of rainfall in a matter of hours, often sparking flash flooding for the affected region(s). For example, in the United States, significant flash flooding events in the Midwest have been attributed to MCS development, where these convective systems form and propagate eastward (Bosart and Sanders 1981). These MCSs shared many common synoptic influences aiding in their formation, such as widespread high moisture content, weak to moderate vertical wind shear, a quasi-stationary frontal boundary, and echo training of convective bands within the MCS (Maddox et al. 1979, Maddox et al. 1980).

The primary source of instability and moisture, at least with regard to United States MCS formation, has consistently been attributed to the existence of a nocturnal low-level jet, where the ingest of warm moist air leads to widespread convective development and precipitation totals (French and Parker 2010; Schumacher and Johnson 2008). To supplement this influx, a quasi-stationary frontal boundary, typically aided by an upper-level trough, provides the vertical uplift required for the low-level flow to realize all of its potential energy (Aylward and Dyer 2010). Other synoptic scale lifting agents, such as mesoscale convective vortices, have also been shown to serve as the source of extreme-rainfall-producing MCSs, albeit these cases are much less common (Schumacher and Johnson 2009).

To apply these common attributes elsewhere around the globe, specifically to the location of this study, MCSs in East Asia have appeared to exhibit similar synoptic ingredients necessary for producing torrential rainfall. In this case, the E-W oriented Meiyu front provides the synoptic scale vertical lift necessary for MCS development, especially in East China (Ding 1994). Studies have shown that the required convective available potential energy and moisture for MCS formation along the Meiyu front comes from the ingestion of low-level southwesterly flow, originating from the Indian Ocean monsoon region (Chen and Yu 1998; Chen et al. 2010; Liu 2010). Once fully developed, MCSs along the Meiyu front produce extreme rainfall totals across the Yangtze-Huai River Basin (YHRB) in excess of 100 mm/day (Qian et al. 2004; Zhang and Zhang 2012), typically resulting in dangerous flash flooding for this region of East China.

On a more resolute scale, convective circulations begin to form within the MCS once the synoptic-scale conditions become less important. These convective cells, aligned in linear bands, are responsible for the bulk of the accumulated precipitation totals, as the highest rainfall rates are found within each convective band. Within each band, the convective cells undergo backbuilding along the leading convective edge, where new convective cells form along the outflow boundary and older cells, now characterized by lighter, more stratiform precipitation, are shifted back towards the center of the MCS (Schumacher 2009). As the convective cells propagate forward, they pass over the same locales one after another, resulting in the aforementioned phenomenon branded echo training (Aylward 2010; Doswell et al. 1996; Schumacher 2009; Schumacher and Johnson 2009).

With echo training typically responsible for the bulk of the extreme rainfall, a similar process known as band training is essential for MCS maintenance as well (Luo et al. 2014). However, unlike echo training, which characterizes the propagation of convective cells within each convective band, band training involves the sequential passage of the larger rainbands themselves. Although this process also adds to the extreme rainfall totals, the linear alignment and passage of each sequential rainband has been shown to primarily be responsible for rainband longevity and linear organization, allowing for each band to ingest warm, moist low-level flow sustaining the MCS convective structure in the most ideal, efficient fashion (Luo et al. 2013).

It is clear from the previous studies mentioned above that the synoptic and mesoscale features of the MCS responsible for extreme rainfall production are well understood conceptually. The current difficulty with extreme-rainfall-producing

MCS research involves the complexity of modeling the important mesoscale features, such as echo and band training, within the MCS. To date, simulations have been able to reach a resolution of 1-5 kilometers, allowing for relatively accurate representations of larger scale convective features such as convective band orientation and general propagation. The smaller convective cell circulations within the bands, on the other hand, have been more difficult to correctly reproduce given their smaller size compared to available model resolutions.

As mentioned in Part I of this series of papers (herein denoted “Part I”) by Zhang and Zhang (2012), model resolution has improved in the past decade, with MCS simulations occurring at grid sizes as low as 2 – 5 km (Wang et al. 2005).

Technological advancements have much improved over the past decade, where earlier simulations occurred at resolutions greater than 10 km (Kato 2006, Zhang and Fritsch 1986). Adding to this difficulty, the lack of high resolution observations during early modeling efforts also hampered simulation attempts. The lack of real data made rainfall distribution totals very difficult to validate, diminishing the significance and usefulness of model precipitation output (Fritsch et al. 1998).

Even when taking into account these lack of resources, some early studies were still able to understand certain MCS features. Many of these studies focused on the Meiyu season (Chen and Yu 1988), which produces enough precipitation to be analyzed on larger (50 km) resolution models. This extreme rainfall along the Meiyu front can be attributed to widespread abundant moisture but low levels of CAPE, relevant to the modeling process due to a smaller emphasis on the model convective parameterizations (Chen et al. 1998; Chen and Yu 1988).

The smaller-scale convective elements within MCSs, that these earlier studies were unable to discern, were not more extensively investigated until models were able to reach resolutions of 1-5 km. Once that level of resolution was achieved, mesoscale convective structures were more successfully resolved and compared at various resolutions within the 1-5 km range in order to evaluate the difference in convective model output. In comparing runs with resolutions of 1 to 2 km with those with 4 km, for example, it was found that the higher-resolution output consistently produced mesoscale convective features most reasonably (Qian et al. 2004; Schwartz 2009). This result is not surprising, as such high resolutions allow model convective activity to be created more explicitly, as opposed to relying more heavily on model parameterization schemes (Lean et al. 2008).

Nevertheless, convective parameterization is still vital to produce accurate model precipitation totals, and improvements should be encouraged as model resolutions continue to shrink (Kain 2004). That process of downscaling convective resolution of mesoscale models has already begun. In Part I of this series of papers, which this study expands upon, a model analysis using a sub-kilometer resolution was introduced to help resolve the smallest convective elements within the MCS structure. The modeling of these convective elements will help build upon what is already understood regarding MCS rainfall intensity and distribution.

## **1.2 Previous Studies of Convective Organization**

The leading convective line of an MCS, typically organized as a linear squall line, contributes significantly to the total MCS rainfall output due to the heavy rainfall

rates produced within. With respect to lateral structure, the most common MCS archetype consists of a strong convective line at the leading boundary with lighter stratiform precipitation trailing behind, the latter making up much of the MCSs horizontal extent. This type, denoted as a trailing stratiform “TS” MCS, is the most common structural type observed (Parker and Johnson 2003).

However, TS MCSs have been recently compared to lesser known structural types - MCSs with leading stratiform “LS” and parallel stratiform “PS” precipitation, to further distinguish the contributing factors that instigate MCS development and organization (Parker and Johnson 2004). One of the main differences between these MCS types derives from the direction of new convective cell formation in relation to the cold pool location. TS MCSs tend to initiate new convection downshear from the outflow boundary, away from the stratiform precipitation and cool outflow, whereas convective activity from LS and PS types may develop in conjunction with the stratiform region, where the outflow boundary may not be propagating away from the stratiform region (Johnson and Parker 2004). The other significant difference is in the direction of the storms mid to upper-level storm relative winds. If these winds are tilted upshear into the interior of the MCS, hydrometeors will be advected and accumulated behind the leading line to grow a TS type system. However, downshear advection of hydrometeors would facilitate precipitation development ahead of the leading line, and an MCS with a LS structure (Parker and Johnson 2004).

The development and maintenance of the convective line, located on the leading edge of the MCS when considering TS-type systems, is crucial for extreme rainfall production and is the culprit for much of the extreme weather associated with squall

lines, i.e. strong straight-line winds and flash flooding. Focusing on TS MCSs, it is understood that the developing squall line is dependent on both the magnitude and orientation (with respect to the leading line direction) of the low-level shear vector. The well-referenced study conducted by Rotunno et al. (RKW, 1988) introduced the theory, herein referred to as RKW theory, that shallow shear from 0 – 2.5 km AGL oriented perpendicular to the convective line may develop into a long-lived line with short-lived multicells making up the line. On the other hand, supercell storms with separated, independent outflows tend to form in deeper shear from 0 – 5 km AGL, where the shear is oriented at more of an acute angle to the convective line (Rotunno et al. 1988).

RKW theory further summarizes that in spite of the strength and direction of the environmental shear, the presence of low-level ambient shear alone is crucial for convective line development (Rotunno et al. 1988). Numerically, it is widely accepted that 0 – 6 km low-level shear values of approximately  $15 \text{ m s}^{-1}$  are ideal for a multicell squall line, as typically seen with a torrential-rainfall-producing MCS, given an adequate amount of positive buoyancy and moisture (Weismann and Klemp 1982). Deeper 0-6 km shear values of  $20 \text{ m s}^{-1}$ , including shear that veers with height, have been found to lead to supercell development, albeit not as commonly associated with MCSs as multicells (Rotunno and Klemp 1982).

### **1.3 Significant Findings From Part I**

Part I of this series of papers introduced an MCS that developed along the Meiyu front during the evening hours of 4-5 July 2003 over the Yangtze-Huai River Basin

(YHRB) region. Responsible for torrential rainfall over the Chuzhou-Nanjing metropolitan region in East China, the event produced 273.5 mm of rain in a 24 h period, nearly all of which occurred during the evening hours (Zhang and Zhang 2012). Part I investigates this torrential-rainfall-producing MCS by examining the synoptic environment required for generation, as well as verifying the accuracy of Mesoscale Model (MM5) nested grid simulations with observed radar, satellite, and rainfall data.

The large-scale atmospheric setup over the Chuzhou region was found to be conducive to MCS production, exhibiting many of the known dynamics needed for heavy rainfall formation. At the Meiyu boundary, cold outflows left behind from a dissipating afternoon MCS met unstable, low-level high- $\Theta_e$  air, advected in from the Southeast Asian monsoon region to the southwest (Zhang and Zhang 2012). The southwesterly inflow acted as a low-level jet, continually supplying the YHRB region with the moisture necessary for widespread convective development and extreme rainfall output.

Satellite, radar, and rain gauge observations provided the visual and numerical observations, respectively, used to confirm MCS propagation and rainfall output. These observations indicated three convective storms which developed in the evening hours - to the west of Chuzhou - between the outflow of the previous afternoon MCS and the Meiyu front. Radar and satellite observations then detailed the subsequent organization of the MCS throughout the early evening, the passage of a leading convective line through Chuzhou around 1700 UTC July 4<sup>th</sup>, and the eastward MCS propagation and dissipation approaching 0000 UTC July 5<sup>th</sup>. The most intense

convective development occurred as the MCS propagated over Chuzhou, resulting in an extreme rainfall total of 273.7 mm over a short 6 hour period during MCS passage.

Using the sub-kilometer simulation (0.444 km) over the smallest domain, Zhang and Zhang (2012) recreated the MCS lifecycle as well as the torrential rainfall production. The MM5 simulation accurately produced the cold outflows associated with the previous afternoon MCS as the evening MCS began to develop. The model also simulated the triggering of the new convective storms along the leading outflow boundary with a high level of accuracy. The sub-kilometer recreation indicated isentropic lifting of the southwesterly inflow as a main cause of early convective initiation with this MCS, as the inflow converged with the residual cool outflows from the afternoon. On a more resolute mesoscale level, the model also correctly indicated the individual convective cells within the larger convective line, responsible for producing localized heavy rainfall. These torrential-rainfall-triggering convective bands were at the right location (over Chuzhou), however, the time of passage was offset by 2-3 hours (Zhang and Zhang 2012).

#### **1.4 Objectives of this Study**

In Part I, Zhang and Zhang (2012) have investigated the large and mesoscale aspects of the extreme rainfall events as well as the trigger of deep convection over a cold pool. In this study (henceforth referred to as Part II), we will focus more on the development of some small-scale convective elements within the larger MCS. Specifically, whereas Part I focused on the synoptic scale environment conducive to MCS development and the formation convective bands therein, which lead to extreme

rainfall, Part II will investigate the formation and propagation of the individual convective cells within the rainbands, as well as a more in-depth analysis of rainband propagation as well. The convective structure of the cells will be examined, as well as the echo and band training associated with localized extreme rainfall. These features will be simulated using the sub-kilometer simulation of 0.444 km, mentioned previously in Part I as the first sub-kilometer simulation used to investigate extreme rainfall production associated with an MCS.

Specifically, the individual objectives of Part II are to: (a) examine the development and organization of localized convective bands leading to extreme rainfall production through echo and band training phenomena; (b) explore the vertical structures within the convective bands during various stages of development, including the interaction of cool outflows with vertical wind shear and CAPE; and (c) closely investigate the structural evolution of one of the convective bands that is responsible for the highest localized rainfall output over the Chuzhou region.

The next chapter provides a detailed description of the model used for this study, including the parameterizations used to calculate important variables. In Chapter 3, rainband and convective cell propagation are presented to help explain the production of extreme rainfall via band training; the atmospheric ingredients aiding in the formation and organization of localized convective bands are discussed; the evolution and distribution of important variable maximums are shown; and the vertical structures of the convective bands are detailed to engage our understanding of how vertical motions influenced extreme rainfall formation. The study will wrap up with

Chapter 4, which will include a summary of results and implications for future studies.

## Chapter 2. Model Description

The Pennsylvania State University – National Center for Atmospheric Research (PSU-NCAR) Mesoscale Model (MM5 Version 3.6), used in Part I as well as this subsequent study, is a quadruply-nested cloud-resolving model with nested grid sizes of 12/4/1.33/0.444 kilometers (Zhang et al. 1986). In reference to the important mesoscale convective processes, such as cloud resolution and subsequent precipitation formation, the two larger grid sizes use both the updated Kain-Fritsch (2004) cumulus parameterization and the Tao and Simpson (1993) three-ice cloud microphysics scheme; whereas the two smaller grid sizes use only the Tao and Simpson scheme. All grid sizes use a modification of the Blackadar planetary boundary layer parameterization (Zhang and Anthes 1982) and a cloud-radiation interaction scheme (Dudhia 1989). The impact of shortwave radiation, longwave radiation, and cloud radiation are all included in the calculation of land surface temperature, which uses the surface energy budget equation. Further details into MM5 parameter calculations can be found in Dudhia (1993) and Grell et al. (1995).

Horizontally, each grid resolution domain consists of (x, y) dimensions  $202 \times 232$  (D1),  $385 \times 391$  (D2),  $385 \times 391$  (D3), and  $385 \times 391$  (D4) while also reaching a vertical level of 30 hPa, containing 40  $\sigma$ -coordinate levels. These levels become more resolute in the PBL and follow uneven terrain across the domain boundary (Zhang and Zhang 2012). As mentioned previously, D4 will remain of greatest relevance to the current study, as it is resolute enough to evaluate the convective processes within the MCS rainbands. The larger domains are more equipped to

evaluate the synoptic level flows governing the development of the entire MCS event, thus leaving it less relevant for the purpose of this investigation.

On a temporal scale, the model is initialized at 0000 UTC 4 July 2003 using the NCEP  $1^\circ \times 1^\circ$  reanalysis, which was enhanced at 6 hour intervals with conventional and field observations in order to produce the most accurate initial and lateral boundary conditions for the model. As D1 is initialized at 0000 UTC 4 July 2003, the initial conditions used for each subsequent smaller domain are extracted from the coarser domain, with D2 activating 6 hours into the integration (0600 UTC), and D3/4 activating 12 hours into the integration (1200 UTC) with all domains ending at 0000 UTC 5 July 2003. The time frame for each respective domain allows for full MCS analysis, as the larger domain integrations cover the entire MCS lifecycle and the coverage of the smaller domains capture the lifetimes of the localized convective bands within the MCS.

## Chapter 3. Convective Structures

### 3.1 Distribution and Evolution of Rainbands

To understand how extreme rainfall was generated in the vicinity of Chuzhou, an analysis of the lateral convective rainband structure is critical. Introducing this rainband structure, Fig. 1 presents the simulated reflectivity (dBZ),  $\Theta_e$  (K), and flow vectors ( $\text{m s}^{-1}$ ) every hour from 1500 – 2000 UTC 4 July 2003, with each frame representing a height of 500 m above ground level (AGL). It should be noted that although the MCS has developed earlier, around 1200 UTC 4 July 2003, and progressed eastward beyond 2000 UTC 4 July 2003, the 5-h window represents the time period where important convective rainbands move into the smallest D4 frame, develop into mature convective bands, produce torrential rainfall in the vicinity of Chuzhou, and move out of the frame and Chuzhou region.

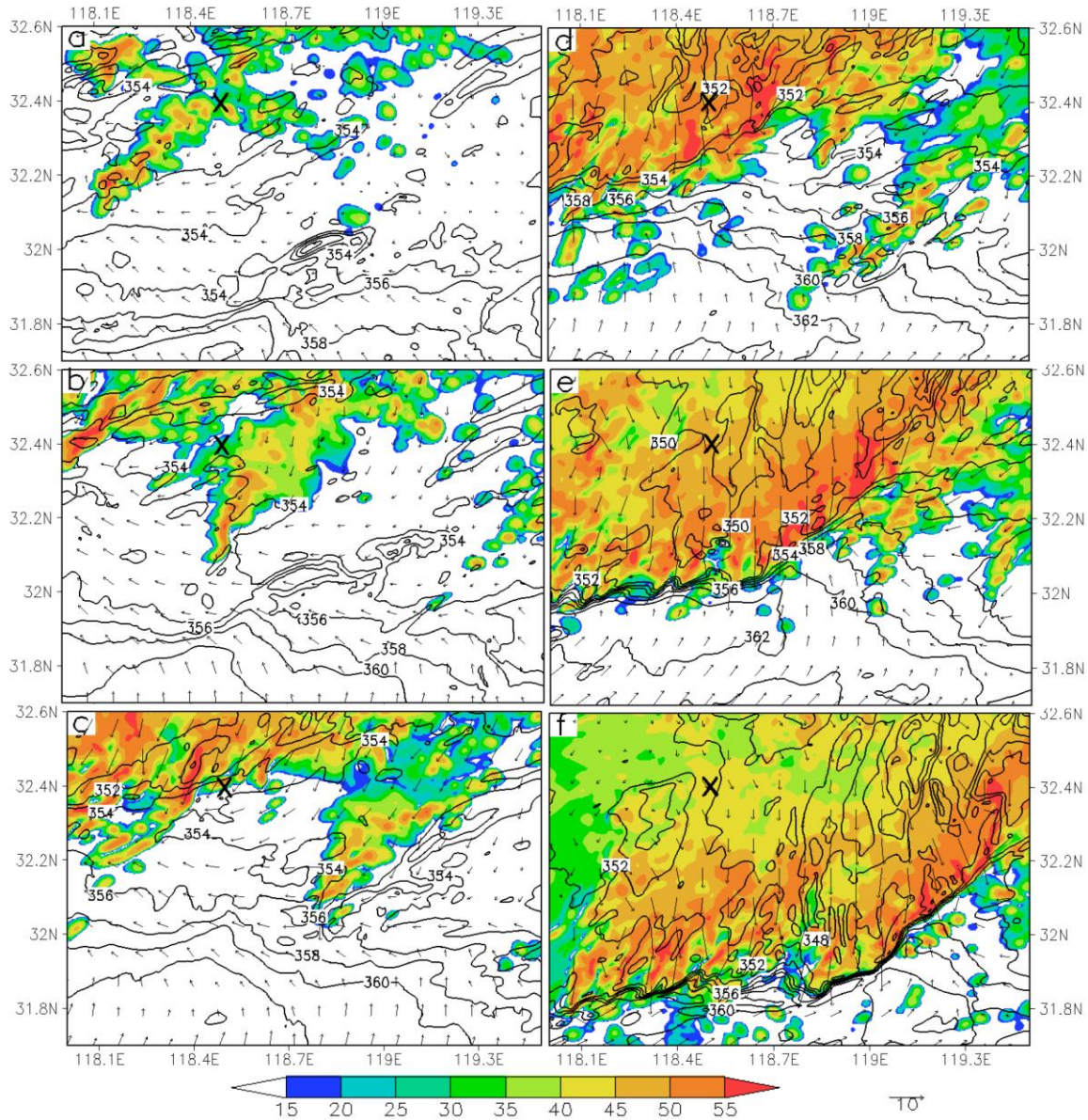


**Figure 1.** Horizontal distribution of flow vectors,  $\theta_e$  (solid contoured at 2K intervals), and radar reflectivity (color shaded) at  $z = 500$  m from (a) 15-h; (b) 16-h; (c) 17-h; (d) 18-h; (e) 19-h; and (f) 20-h simulations over D4. 'X' denotes the location of Chuzhou.

At 1500-1600 UTC (Figs. 1a,b), a line of weak convective cells, noted from the lack of high reflectivity values, moves eastward into the frame and towards Chuzhou. This initial band is oriented in SW-NE fashion, and foreshadows the general orientation of the stronger convective bands to follow. In Fig. 1a, the environmental

flow ahead of this convective line is from SE, and it may be inferred at this convective boundary that the warm air is helping develop the prominent SW-NE convective band, as the flow is perpendicular to the line orientation. Transitioning to Fig. 1b, this convective band has moved farther east, with the strongest cells within the line passing just south of Chuzhou, albeit still likely responsible for some measurable rainfall total. However, this line hasn't appeared to intensify, as the lack of stronger reflectivities within the convective cells as well as the absence of a significant  $\Theta_e$  boundary indicates a lack of strong precipitation and outflow development. Aside from this initial band, a stronger convective band appears in the top left of Fig. 1b, and becomes the focus of the subsequent hourly frames of Fig. 1.

Moving on to Fig. 1c, the convective band first noted at the top left corner of Fig. 1b has propagated eastward towards Chuzhou. With regard to orientation, this band is also directed in a general SW-NE fashion, albeit slightly more N-S than the first rainband. The significance of this band, however, is the propagation with respect to the location of Chuzhou and the intensification of convective development. Unlike the first band which passed slightly to the south, the strongest regions of this second rainband prepare to pass over the Chuzhou region directly. The band has begun to transition into the mature stage of convective development, as indicated by the very high reflectivity values (55+) and strong southeasterly inflow, although a significant  $\Theta_e$  gradient has yet developed. Fig. 1d shows the convective orientation one hour later (i.e., at 1800 UTC), thus indicating the strong convective band passed through Chuzhou sometime between 1700-1800 UTC. The larger coverage of the MCS can be seen in Fig. 1d as well, as a large area of stratiform precipitation is shown behind

this second convective band. This stratiform region is now present over Chuzhou, with embedded areas of stronger precipitation, indicated by stronger reflectivities, propagating through and adding to extreme rainfall totals.

Even though the second convective band has passed by Chuzhou, the band continues to develop into a strong leading squall line, as indicated in Figs. 1e-f. The convective line has spread laterally, still along an SW-NE direction, with a thorough convergence boundary where the southeasterly inflow meets the now well-developed northwesterly convective outflow. Consistent with the well-developed outflow boundary is a considerably strong  $\Theta_e$  gradient of around 8-10 K along the leading convective line, indicating a stark contrast between the precipitation-loaded cool outflow and the warm inflow ahead.

Another important feature of the convective bands during this mature stage is the subsequent convective bands that follow behind the southern end of the leading convective line. These bands show the same linear SW-NE orientation that the earlier convective bands also displayed, and a strong  $\Theta_e$ -gradient is also apparent at their boundary with the environmental flow to the south, indicating the boundary between the MCS outflow and environmental inflow is helping to develop these convective bands. As these bands propagate eastward, they each unload heavy precipitation upon the affected regions, altogether creating extreme rainfall totals within a few hours. This phenomenon, previously described as band training, appears to be responsible for much of the accumulated precipitation around the Chuzhou region.

To further understand how these rainbands generated and contributed to extreme rainfall, Fig. 2 illustrates the 20-minute rain rate associated with each rainband that

passes through the Chuzhou region. In this set of 20-minute figures, “X” again denotes the location of Chuzhou, and each relevant rainband is denoted with the letters A-E. For each frame the contours lag the shaded reflectivities by 20 minutes, indicating that the corresponding reflectivities show the convective band locations at the end of the 20-minute rain rate interval. Of greatest significance to rainfall production is rainband B, corresponding to the second rainband discussed in Fig. 1 which passed through Chuzhou shortly after 1700 UTC 4 July 2003.

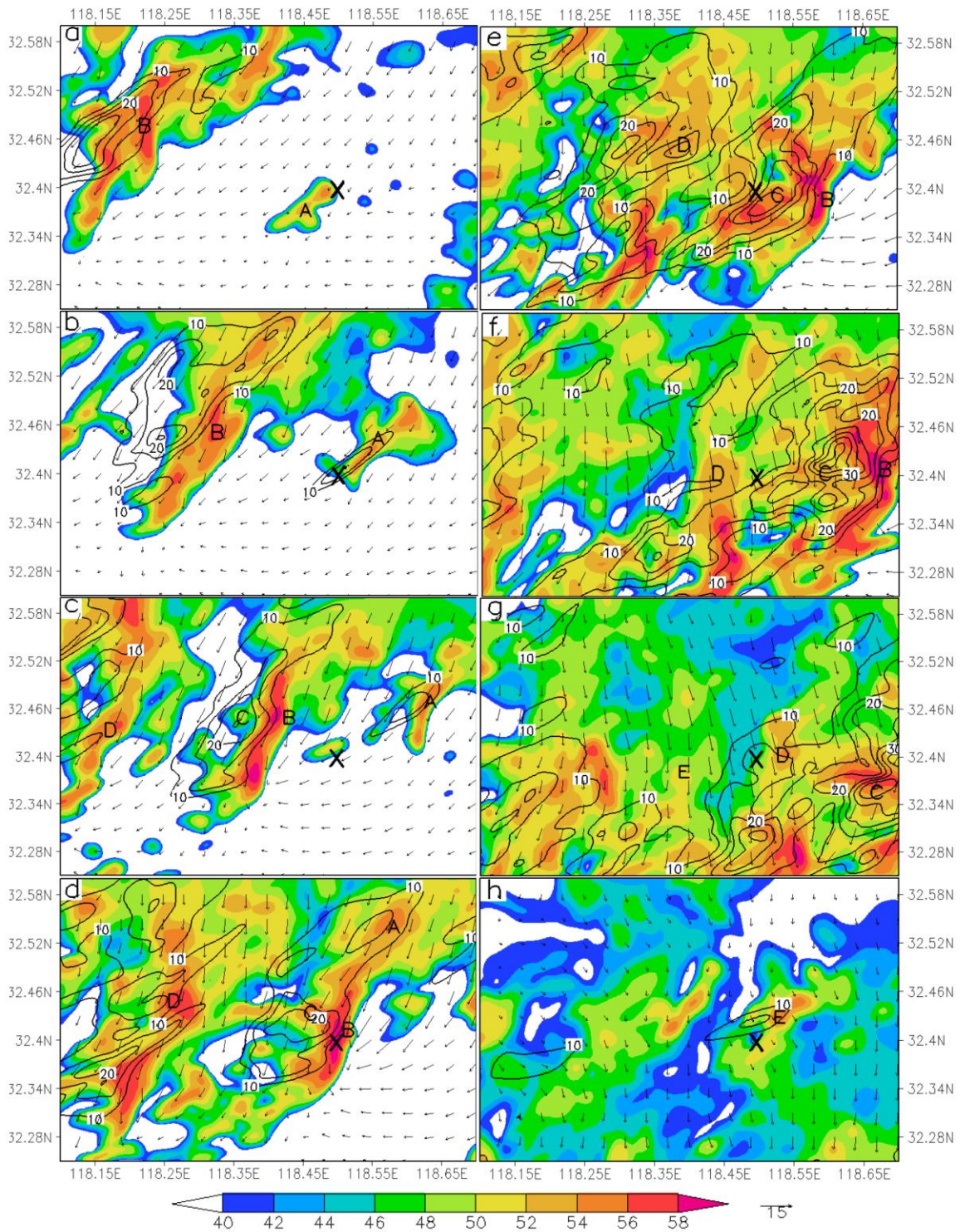


**Figure 2 :** Simulated surface reflectivity (mm shaded), 20 min rainfall (contoured, 5mm intervals), and storm-relative surface flow vectors at (a) 1620Z, (b) 1640Z, (c) 1700Z, (d) 1720Z, (e) 1740Z, (f) 1800Z, (g) 1820Z, and (h) 1920Z. Convective cells A, B, C, D, and E denote relevant convective cells, with 'X' representing the location of Chuzhou.

Figs. 2a-b show the first two convective cells, i.e., bands A and B, that affect Chuzhou. Band A, too small in size to be easily recognizable in Fig. 1, appears as a small cell in the front of rainband B. Fully located within the moist environmental flow ahead of the MCS boundary, this cell passes through Chuzhou between 1620-1640 UTC, with a 20-minute rain rate of roughly 10-15 mm rainfall. Fig. 3, which displays the 20-minute rain rate at the location of maximum rain rate (red) and maximum rainfall accumulation (blue), both of which are located within the vicinity of Chuzhou, shows agreement with the rain rate contours of Fig. 2 with a rain rate peak of 15 mm per 20 minutes at 1640 UTC. Moving in a SW-NE direction, cell A does not propagate eastward with the MCS or other convective bands, thus appearing to act as an isolated air mass thunderstorm instead of a rainband formed through MCS dynamics. Rainband B is also apparent in Fig. 2a-b, propagating eastward and approaching the Chuzhou region.

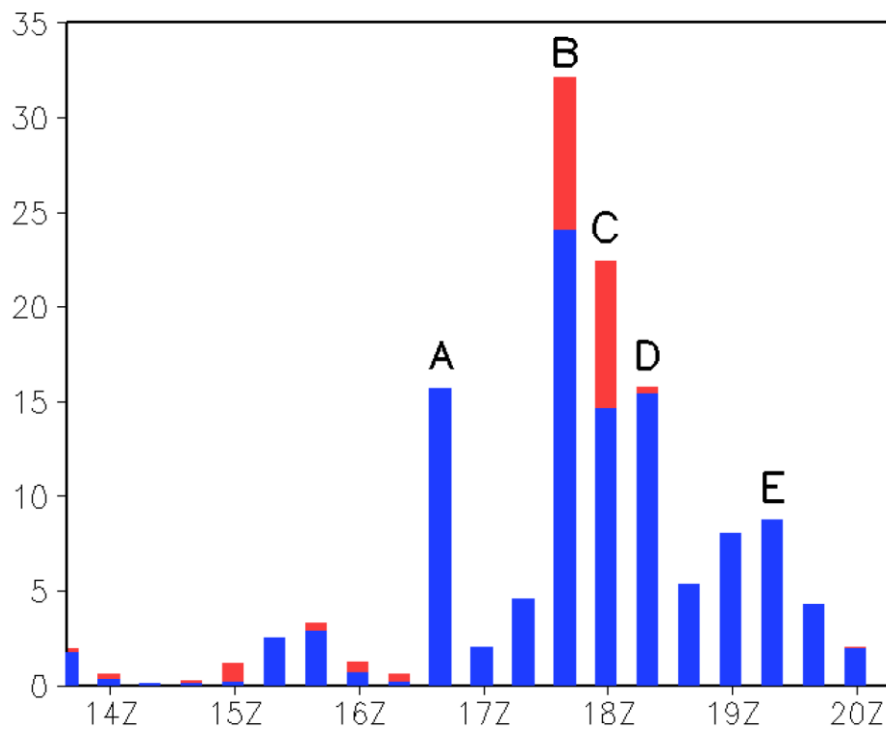


**Figure 3 :** 20-min rain rate (mm) time series at the point of maximum 24 hour (00Z 4 July 2003- 00Z 5 July 2003) rainfall accumulation (blue - 32.41°N, 118.51°E) and the point of maximum rain rate (red - 32.375°N, 118.5 °E) over D4 during the 24 hour period. A, B, C, and D represent convective cells relevant to extreme rainfall totals.

The influence of rainband B, as well as other subsequent convective cells, can be seen in Figs. 2c-e from 1700-1740 UTC. During this period, cell A has fully moved away from Chuzhou and has been overwhelmed by and assimilated into the larger MCS convective structure. Of most importance during this period is the passage of rainband B at 1720 UTC, which is subsequently associated with 20-minute rain rates of greater than 30 mm. The analysis of rainband B is in agreement, both in terms of the arrival time of the rainband at Chuzhou and rainband's precipitation intensity, when comparing Figs. 2-3. Fig. 3 confirms the passage of the rainband shortly after 1720 UTC, with the extreme rain rate plotted at 1740 UTC. The value of this extreme rainfall also appears to indicate a maximum slightly greater than 30 mm per 20 minutes, again cooperative with the rain rate contours in Fig. 2.

Other embedded convective waves are also apparent in Figs. 2c-e, notably bands C and D. These bands do not appear to be as convectively rigorous as rainband B, as they show weaker reflectivities and lower trailing rain rate values of about 20 mm and 15 mm, respectively. Band C appears to pass over Chuzhou shortly after rainband B at 1740 UTC, which is also shown in Fig. 3 as the rain rate total of 20-25 mm per 20 minutes at 1800 UTC. After band C, band D passes through Chuzhou shortly after 1800 UTC as indicated in Fig. 1f. This convective cell produces 20 min rain rates of roughly 15 mm, as can be seen in Fig. 3. The final convective band passing over Chuzhou and contribute to extreme rainfall is band E, displayed in Figs. 1g-h. This band is difficult to discern in Fig. 1g, as it appears embedded in the trailing stratiform region with a reflectivity no greater than 52 dBZ. Moving northeastward, rainband B impacts Chuzhou shortly before 1920 UTC (Fig. 1h) with rain rate totals of approximately 10 mm per 20 minutes and reflectivity values approaching 56 dBZ.

Collectively, the passage of convective bands A-E help explain the extreme rainfall produced at Chuzhou during MCS passage. We can see from this analysis that each convective band propagates past the Chuzhou region consecutively, exhibiting band training motion mentioned previously, with each cell contributing to the extreme rainfall total. Tracking these rainbands help determine the aforementioned precipitation totals, but why the convective bands formed, and the orientation which they organized, will involve the evaluation of the environmental characteristics needed for organized, convective development.

### 3.2 Formation and Orientation of Rainbands

For fundamental convective development, the essential ingredients needed for heavy rainfall production are deep positive buoyancy to initiate vertical motion as well as high moisture content for widespread cloud droplet and subsequent precipitation formation. Fig. 4 illustrates one such ingredient, the low-level CAPE present in D4 as the leading line propagates eastward. Low-level CAPE is shaded, with vertical motion contoured and the location of the leading convective edge of the MCS denoted with a thick dashed line.

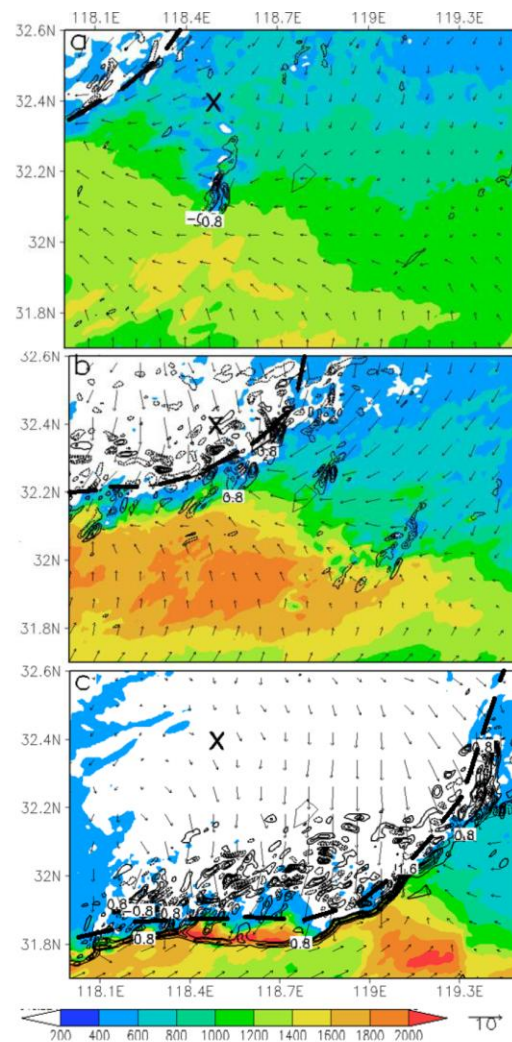


**Figure 4.** Horizontal distribution of CAPE ( $\text{J kg}^{-1}$ , shaded), vertical motion ( $\text{m s}^{-1}$ , solid/upward, dashed/downward), and flow vectors at  $z = 1$  km for (a) 16-h, (b) 18-h, and (c) 20-h. CAPE maximized at 966 mb. Heavy dashed line represents leading edge of 40+ dBZ.

Convective activity can also be inferred from the low-level vertical motion contours, which become stronger and more frequent from Figs. 4a-c. In Fig. 4a, the leading line enters the frame but has not yet infiltrated the more unstable air to the south. However, in Fig. 4b, stronger levels of CAPE, combined with a strong southerly inflow, help build convective activity along the leading edge, as more pockets of vertical motion can be seen along the edge as well as slightly behind.

Two hours later, at 2000 UTC in Fig. 4c, the relationship between the environmental CAPE and convective activity is the most clear. CAPE values of up to 2000 J/kg straddle the leading edge of convective development, which may be considered significant given the typically stable lower troposphere during overnight hours (due to radiational cooling). The leading convective line appears to extend SW-NE and bends more W-E at the southerly end, consistent with the convective organization from Fig. 1. A strong narrow band of vertical motion extends along the length of the boundary, indicating strong convergence and uplift above the convective outflow. Smaller pockets of vertical motion can be found deep behind the leading edge as well, indicating bands of heavier convective development and precipitation formation, contributing to band training and extreme precipitation totals as the MCS propagates eastward.

Although moderate to high convective potential energy and abundant moisture help explain thunderstorm development and precipitation formation, these variables do not help explain why the convective bands formed linearly and consecutively, leading to band training induced extreme rainfall. In order to understand why these

bands organized in a SW-NE fashion as shown in Fig. 1, the hodograph in Fig. 5a is presented to illustrate the low-level environmental shear which is commonly responsible for long-lived convective organization.

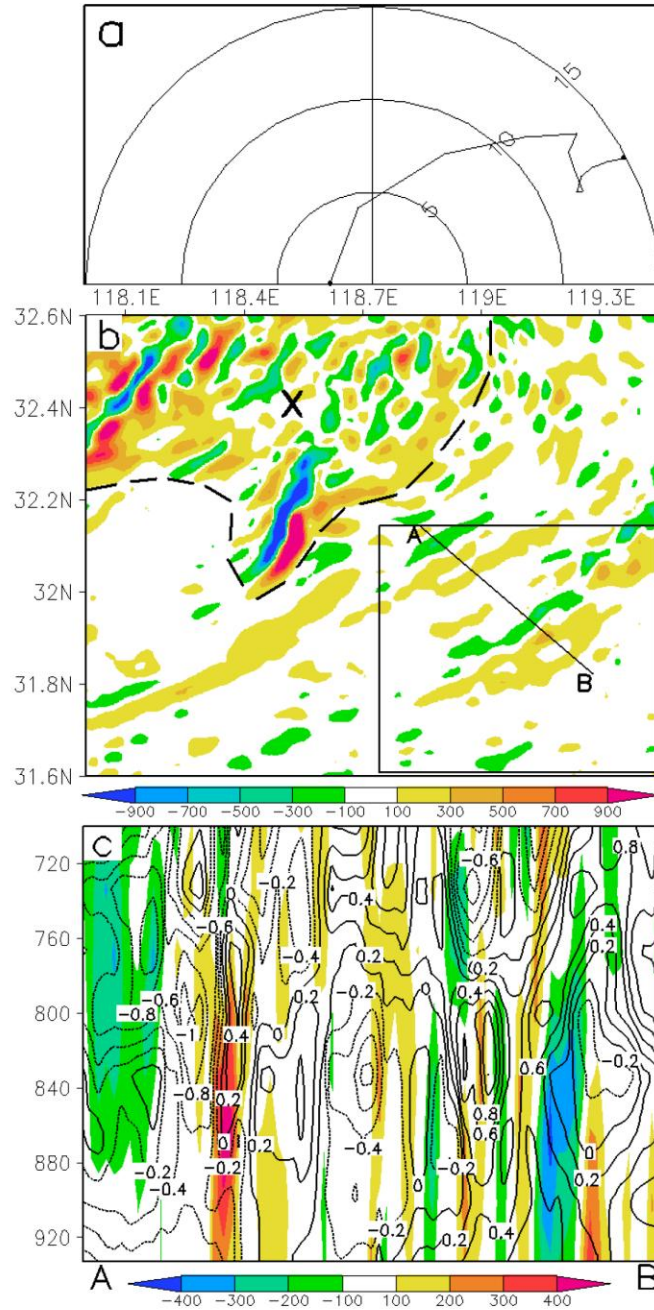


**Figure 5:** (a) Area average hodograph ( $\text{m s}^{-1}$ ) in the lowest 400mb at 16-h (b) 16-h 1 km vertical motion ( $\text{mm s}^{-1}$ ). Solid black line represents leading convective edge at 20+ dBZ. The square box within represents the area average for (a), while the west-east cross section is shown in (c). (c) Vertical cross section of vertical motion (shaded –  $\text{mm s}^{-1}$ ) and  $\Theta$  perturbations (contoured at 0.2 K) taken normal to the shear vector in the lowest 3-5 km of the pre-storm environment from the 16-h simulation over subdomain D4.

Taken in the lowest 400 mb of the boundary layer, the shear vector is oriented in a general SW-NE direction, revealing a southwesterly flow that increases in magnitude from the surface up to the middle troposphere where the flow is roughly 15 m/s. A southwesterly shear vector would thus indicate boundary layer roll circulations to form in a SW-NE orientation as well, as these roll vortices generate parallel to the low-level shear (LeMone 1973; Moeng and Sullivan 1994; Young et al. 2002).

The overturning vertical circulations of the rolls are visible in Fig. 5b, where vertical motion in the vertical 1-km extent is presented over the entire domain with “X” displaying the location of Chuzhou and the dashed black line representing the leading convective boundary. As expected, the strongest vertical motion values of up to  $9 \text{ cm s}^{-1}$  are found right along or slightly behind the MCS leading boundary, where convectively produced vertical motions are greatest. However, of equal importance are the streaks of upward (red, yellow shading) and downward (green, blue shading) motions in the clear air ahead of the MCS. These SW-NE oriented vertical motion bands also owe their organization to the southwesterly low-level shear vector; however, the lack of adequate convective initiation far ahead of the MCS boundary results in simple cloud formation as opposed to thunderstorm development. A cross-section taken perpendicular to the shear vector, indicated as A-B in Fig. 5b, is displayed in Fig. 5c. Taken through the boundary layer rolls ahead of the MCS, the cross section displays the alternating upward (again red, yellow shading) and downward (again green, blue shading) motion near the surface. To relate the vertical motion to buoyant overturning,  $\Theta$  contours generally show the warmer, positively buoyant air rising, while the cooler columns of air sink.

As previously stated, this organizational process is also responsible for the orientation of convective generation along the MCS boundary, not just in the clear air out ahead, as these convective rolls are able to develop into mature thunderstorms seen along the southern end of the MCS in Figs. 1e-f due to the presence of adequate CAPE, moisture, and convergence at the outflow boundary. Each roll-induced convective band is responsible for some sizeable precipitation output, as each band propagates eastward and collectively adds to extreme final rainfall totals. This is again an example of band training within the MCS, as mentioned previously with the convective bands that pass over Chuzhou directly (Fig 2) and further providing evidence that band training was responsible for extreme rainfall totals.

With regards to the CAPE, moisture, and shear discussed previously, these variables are also illustrated from the simulated skew-T/Log-P diagrams of Fig. 6. Each diagram displays the representative atmosphere ahead of, at and behind the convective line, as indicated in the map at the top left.

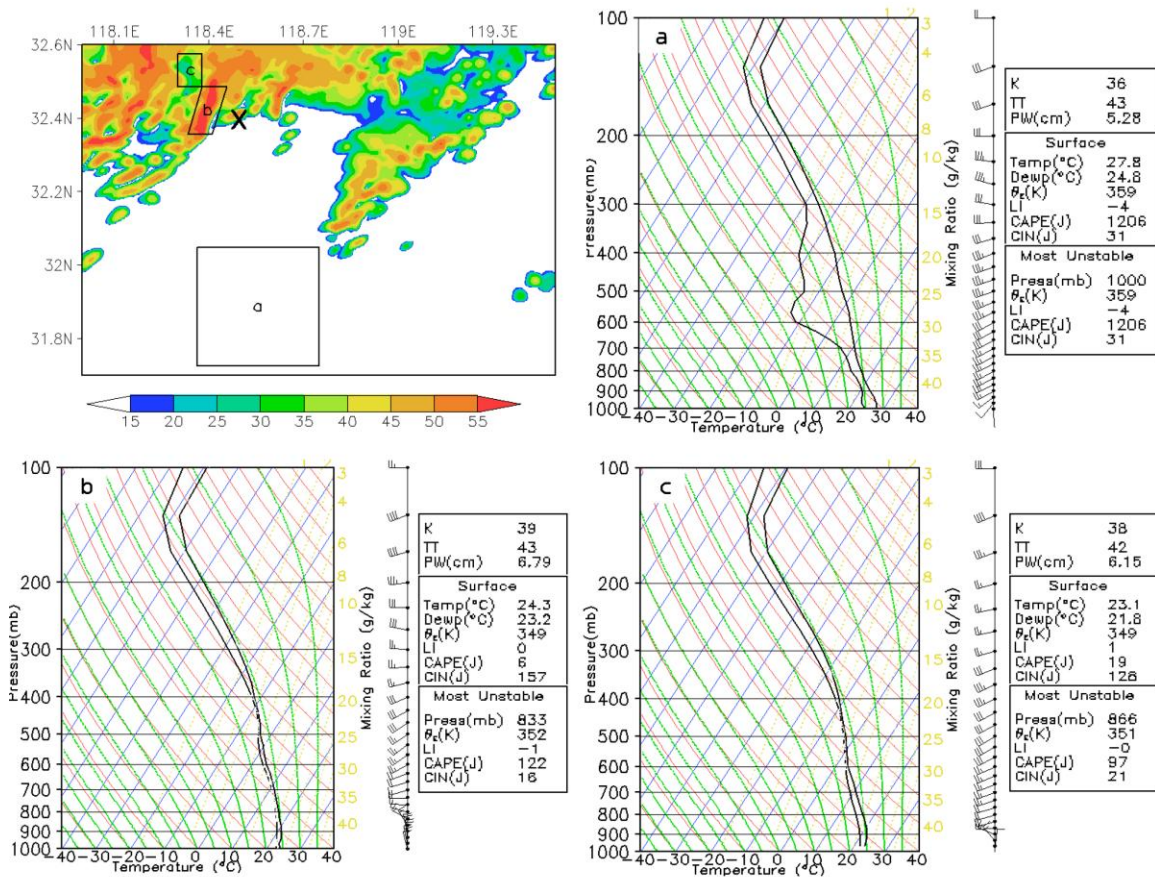


Figure 6. Area averaged skew-T/log-P diagrams taken (a) ahead of; (b) at the leading convective line (location of updraft/reflectivity); and (c) in the training stratiform region from the 17-h simulation. Soundings are averaged over 5 equidistant points within each indicated region at the top left reflectivity map.

Fig. 6a, showing the area-average skew-T/Log-P ahead of the MCS, reveals not only the vertical distribution of CAPE but also the vertical extent of water vapor contained in the air, as the profile is nearly pseudoadiabatic from the surface to the tropopause. The exception to this, a mid-level dry pocket at 600-400 mb, may be indicative of mid-level low  $\Theta_e$  inflow often found at strong convective boundaries. The wind profile for Fig. 6a shows mostly straight-line shear with wind speeds up to 25 kts, and the combination of this shear with deep moisture and warm surface temperatures supports the development of widespread organized convection.

At the leading convective line and behind, respectively, Figs. 6b and 6c show the vertical profiles at the updraft maximum and stratiform region. Both show a nearly saturated vertical column, supporting the heavy rainfall observed over the Chuzhou

region. The only appreciable difference between Figs. 6b and 6c is the wind profile, namely Fig. 6b shows a strong backing pattern at the surface implying the presence of slight cold air advection. This observation is intuitive given that the cool convective outflow pushes into the environmental air out ahead cooling the air as the leading convective line moves forward.

### **3.3 Evolution of Variable Extremes**

To produce such heavy rainfall rates near the vicinity of Chuzhou, some meteorological parameters essential to convective development and subsequent extreme rainfall must intensify to maximize the convective features within the MCS rainbands. For this reason, Figure 7 shows the evolution of four such variables along the leading convective line of the MCS, which provided the bulk of the rainfall at Chuzhou: vertical velocity and convergence (Fig. 7a) as well as cloud hydrometeors (7b). Each graph shows how the maximum value of each variable along the leading convective line (where these variables will be greatest) changes as the leading line intensifies.

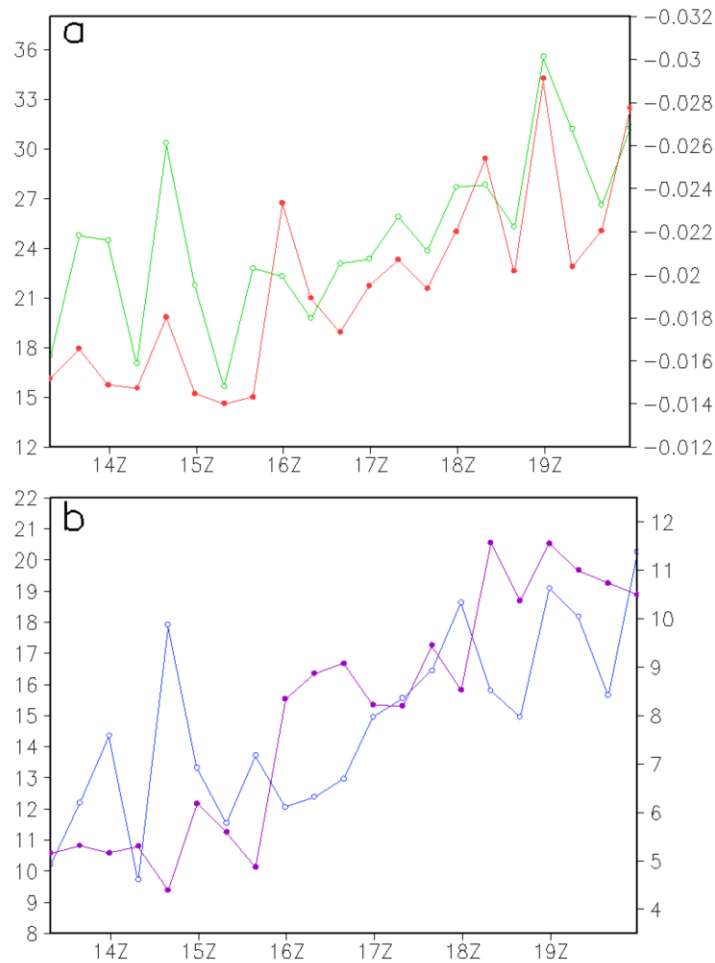


**Figure 7:** Time series of (a) the peak updraft ( $\text{m s}^{-1}$ , green, y-axis on left) and the peak convergence ( $\text{s}^{-1}$ , red, y-axis on right), and (b) the peak cloud hydrometeors ( $\text{g kg}^{-1}$ , blue, y-axis on left) and the peak integrated hydrometeors (cm, purple, y-axis on right). Each time series covers 13 – 20 h over D4 simulation.

In Fig. 7a, the correlation between convergence and resultant vertical motion is visualized. There appears to be no significant time lag between the two, as converging air at the convective boundary forces the flow immediately upwards over the cool outflow. Both variables increase with time and help deepen convective activity at the leading MCS edge, with peak convergence of  $-0.3 \text{ s}^{-1}$  and a peak updraft of  $36 \text{ m s}^{-1}$  found at 1900 UTC when the leading convective line has reached peak strength.

In general, as the magnitude of convergence and vertical motion increases in Fig 7a, hydrometeor loading also amplifies, as can be understood from Fig. 7b. Showing both the location of (three-dimensional) peak hydrometeors and (two-dimensional) column integrated hydrometeors, Fig. 7b indicates that the dynamic convective growth of Fig. 7a helps strengthen hydrometeor loading within the convective bands, as strong vertical motion keeps hydrometeors suspended, allowing for longer droplet growth times. Thus, hydrometeors appear to be maximized around 1900 UTC as well, with peak cloud hydrometeors of 20 g/kg and peak column integrated hydrometeors of nearly 12 cm. Although there is a slight oscillation within 20-minute intervals for each variable in Fig. 7, owing to small-scale variability in convective circulations, the steady trend is for each maximum value to increase, strengthening the dynamic and thermodynamic properties, all of which happen to occur within the leading convective line.

Since Fig. 7 shows how the maximum value of each variable increases as the leading line develops, it does not give an indication of vertical locations and evolution of the variable extremes. Fig. 8, therefore, shows the vertical profile for vertical motion (Fig. 8a) and cloud hydrometeors (Fig. 8b) taken at only 5 selected times during peak development, for visual clarity.

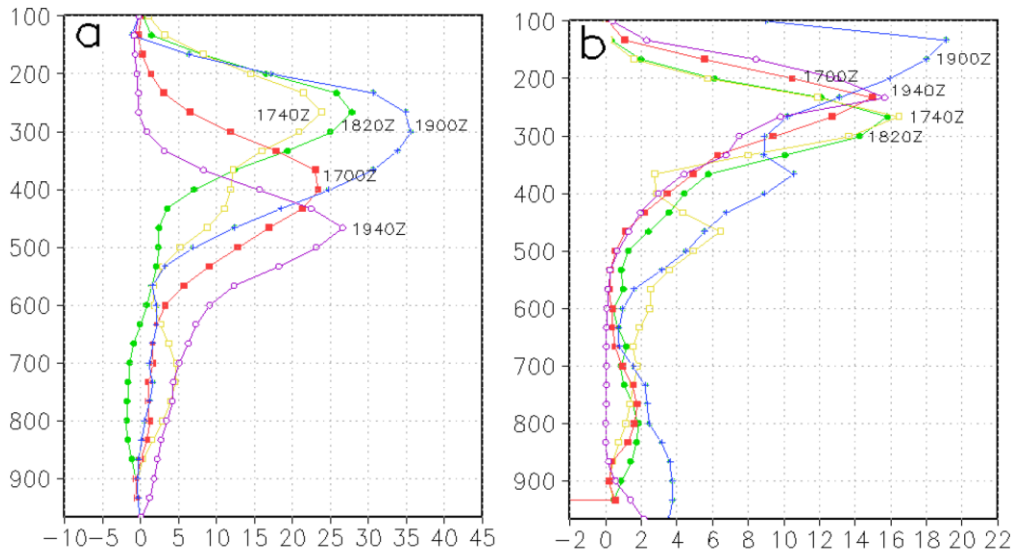


**Figure 8:** Vertical profiles of maximum (a) vertical motion and (b) cloud hydrometeors at each color coded time over D4 simulation. X-axis denotes variable value, whereas y-axis denotes isobaric height (mb).

An examination of each graph in Fig. 8 reveals two overall important trends that appear consistent with each variable. The first trend is that each variable's maximum is slightly higher than what might be expected. Both vertical velocity and cloud hydrometeors have their maximums in the upper troposphere, anywhere from 500-100 mb, where the strong updrafts in the upper levels are advecting lighter hydrometeors into cumulonimbus clouds. Another important result from these figures is the time evolution of the vertical velocity extremes in Fig. 8a, where the strongest updraft appears to decrease in height over time. Generally, the updraft of a mature storm will begin to tilt, accounting for part of this height decrease. However, the gradual loading of hydrometeors in the cumulonimbus cloud and subsequent downdraft development works to lower the updraft height, as the hydrometeor-loaded downdraft begins to overtake the updraft.

### **3.4 Evolution of Rainband Vertical Structures**

An analysis of the lateral propagation of MCS rainbands and of convective variables essential for convective initiation have so far helped us understand how extreme rainfall was produced through band training of convective lines. However, the vertical structures of the convective cells within the rainbands will in their own right help explain how rainfall was generated, as the latent heat released by the storms updrafts influence hydrometeor loading and precipitation formation. The subsequent cool outflows produced from falling precipitation then help to strengthen the already present convective initiation, inherently increasing precipitation totals as storm lifetimes are extended.

In terms of understanding extreme rainfall production induced from band training, it will be important to observe the vertical structure along the band, as individual convective cells may influence each other with shared updrafts and/or hydrometeor transport, as well as the vertical structure normal to the band to best visualize the interaction between the inflow and the MCS outflow. Beginning with the along band structure, Fig. 9 shows along-line cross-sections at 1640 UTC and 1720 UTC, respectively.

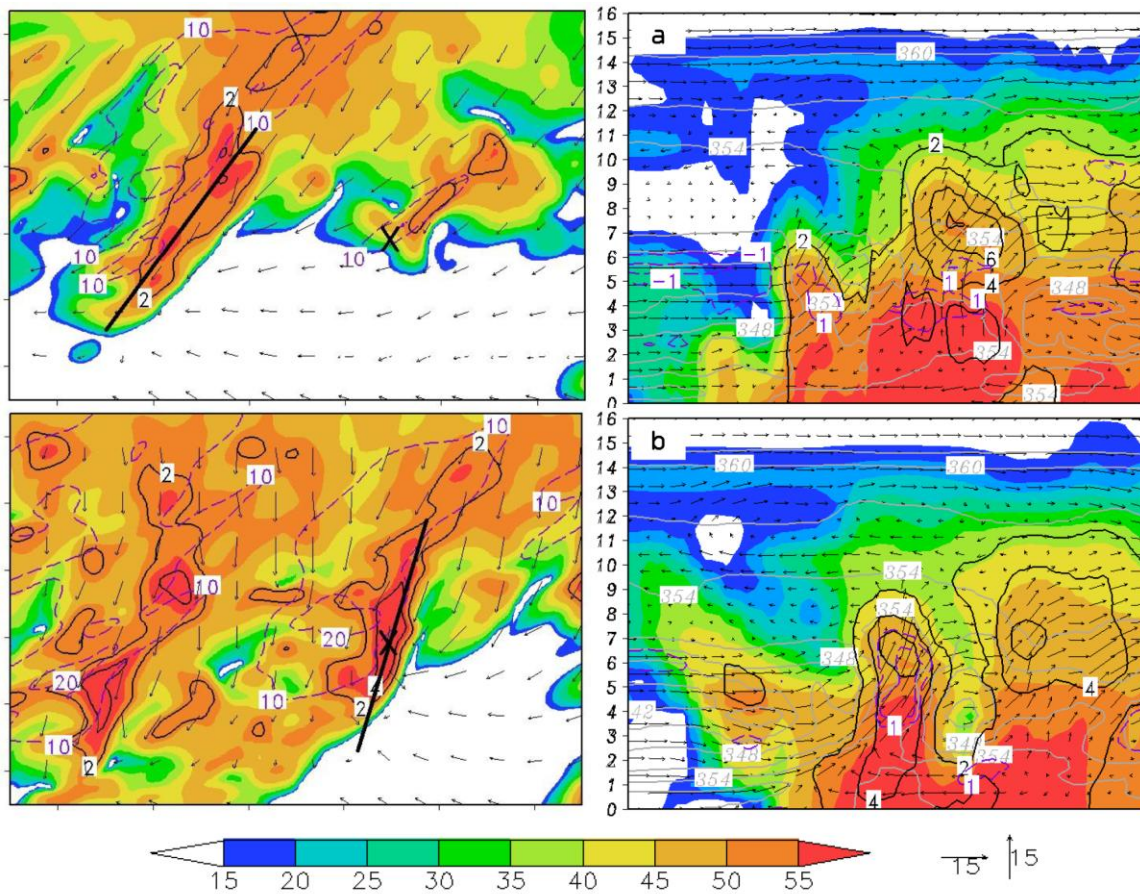


**Figure 9:** Along line cross-sections of simulated reflectivity (dBZ shaded), cloud hydrometeors ( $2.0 \text{ g kg}^{-1}$  black contour intervals),  $\Theta_e$  (3 K grey contour intervals), and temperature perturbations (1 K purple dashed contour intervals), superimposed with in-plane flow vectors at (a) 1640Z and (b) 1720Z. Plan view maps on left indicate cross-section locations, with 'X' denoting the location of Chuzhou.

The band chosen through which to take the cross-sections may be identified as the previously discussed rainband B in Fig. 2, responsible for the bulk of rainfall experienced at Chuzhou, again denoted by “X”. Fig. 9 is representative of the rainband before it reaches the Chuzhou region, and the plan view maps display the integrated hydrometeors and rainfall distributions, as the hydrometeors (contoured black) straddle the heaviest convective reflectivities and the rainfall (contoured purple), due to the time lag, is located slightly behind the convective center.

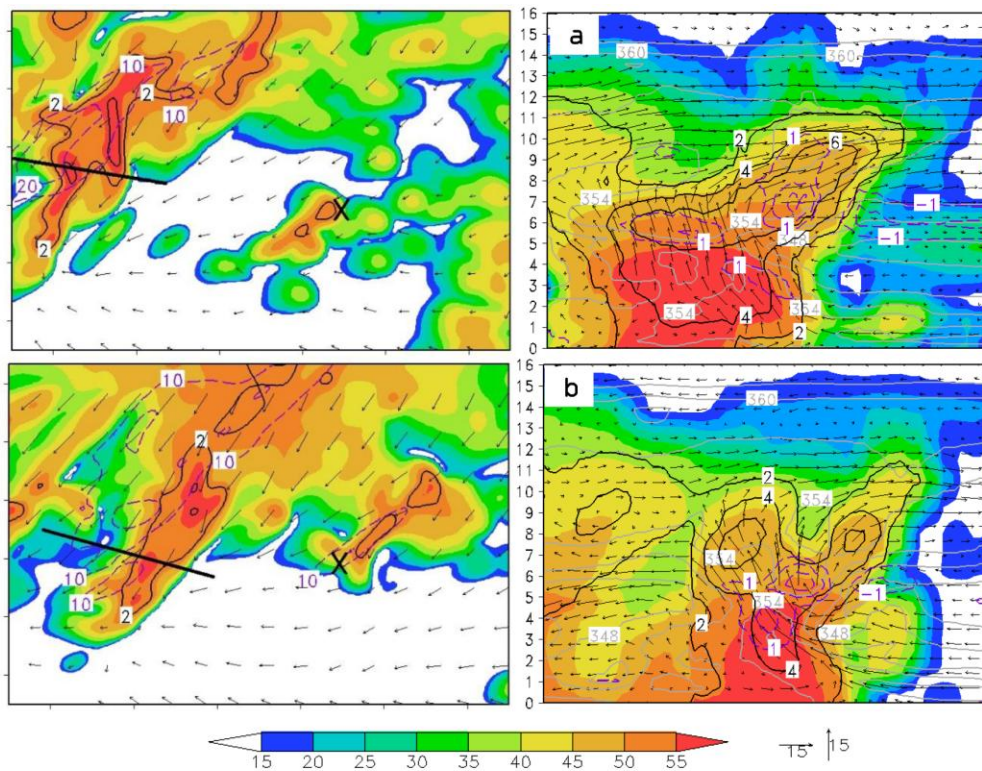
Vertical cross-section in Fig. 9a, taken through the center of the band, shows how these variables are distributed vertically throughout. First taking note of the flow field, a tilted updraft initiating from the southerly environmental flow helps feed CAPE into new convection at the southern end of the band, as the convective centers appear to grow larger towards the band's center. These stronger cells also contain the greatest hydrometeor concentrations of 6-8 g/kg, indicating that precipitation output may vary within the convective band. Thermodynamically, the temperature perturbations and  $\Theta_e$  field do not show significant temperature or moisture gradients, respectively, as the rainband is still in the developing stage.

Fig. 9b shows a cross-section through rainband B 40 minutes later, right as the rainband passes over Chuzhou, as seen on the plan view map. By now, the southerly environmental inflow has strengthened, both in terms of overall speed shown by the flow vectors and in depth, as the flow extends up to 5 km. Although the uplift into the convective band is still tilted into the center, the flow vectors indicate a slightly more vertical uplift along the tilted updraft at each convective cell. The increased latent heat release associated with stronger rising air is shown by more widespread hydrometeor loading, which appears to extend down to the surface in the center cell, providing evidence for precipitation accumulation at the ground. At this time, mid-level low  $\Theta_e$  is also apparent, which is ingested into the convective band helping to enhance negative buoyancy, and the resultant outflow, within the rainband.

Aside from the development of these individual convective variables, these along-line cross-sections through the convective band illustrate the echo training process, which would supplement the precipitation totals arisen from the band training

previously discussed. Comparing the cross-sections from Figs.9a and 9b reveals that the weaker cell at the southern end of the band has the potential to strengthen due in part to the stronger cells outflow boundary forcing the environmental flow up the weaker cell's southerly boundary. By the time the band reaches Chuzhou in Fig. 9b, this weaker band has now become the dominant cell, with the once dominant cell appearing weaker and more stratiform. The regeneration of convective cells in this fashion, known as echo training, occurs within the convective band as it propagates eastward through Chuzhou. Thus, although band training appears to be responsible for the bulk of extreme rainfall produced, echo training of cells within the convective bands only help to add to the high precipitation totals.

In addition to showing along-line cross-sections illustrating the effects of echo training, cross-sections taken normal to the leading line will more clearly indicate the convective inflow/outflow dynamics found at the leading convective line, as these two flows converge with each other right at the convective boundary. These cross-sections are taken through the same rainband as the previous along-line cross-sections as it approaches and passes through Chuzhou, when the convective features are optimized and most representative of extreme rainfall. Fig. 10a shows the cross-section through the rainband at 1620 UTC, where convective activity is in full effect, but the rainband has not organized into a strong, linear convective line.



**Figure 10:** Normal cross-sections of simulated reflectivity (dBZ shaded), cloud hydrometeors ( $2.0 \text{ g kg}^{-1}$  black contour intervals),  $\Theta_e$  (3 K grey contour intervals), and temperature perturbations (1 K purple dashed contour intervals), superimposed with in-plane flow vectors at (a) 1620Z and (b) 1640Z. Plan view maps on left indicate cross-section locations, with 'X' denoting the location of Chuzhou.

At this time, convergence at the surface initiates strong widespread inflow and vertical motion throughout the cell, as hydrometeors of  $6+ \text{ g/kg}$  accumulate in the upper levels. Still in the developmental stage, this cell appears dominated by updraft and without a well-defined, downdraft-driven outflow. The cold pool becomes more apparent in Fig. 10b, illustrating the normal cross-section through the band 20 minutes later at 1640 UTC. The inflow has strengthened, in terms of both intensity and depth, with warm-moist air rising into the cell from the surface. Higher concentrations of hydrometeors ( $6+ \text{ g/kg}$ ) are now more prominent throughout the cells depth resulting from the increase of latent heat release and condensation within

the cell. Mid-level low  $\Theta_e$  inflow is also now more prominent in the mid-levels, feeding into the convective line and aiding to the negatively buoyant sinking, cool outflow.

These same features are apparent as the rainband moves through the Chuzhou region in Fig. 11a at 1720 UTC. The cold pool has deepened further, with the strength of the cold pool roughly equal to the strength of the opposing environmental flow, allowing for a nearly vertical updraft along the leading convective line. Cloud hydrometeor concentrations of up to  $6 \text{ g/kg}$  still extend from the middle to upper levels of the convective cell down to the surface where heavy precipitation is likely falling at Chuzhou. A strong inflow of mid-level low  $\Theta_e$  air still persists, helping sustain the negatively buoyant downdrafts within the convective band.

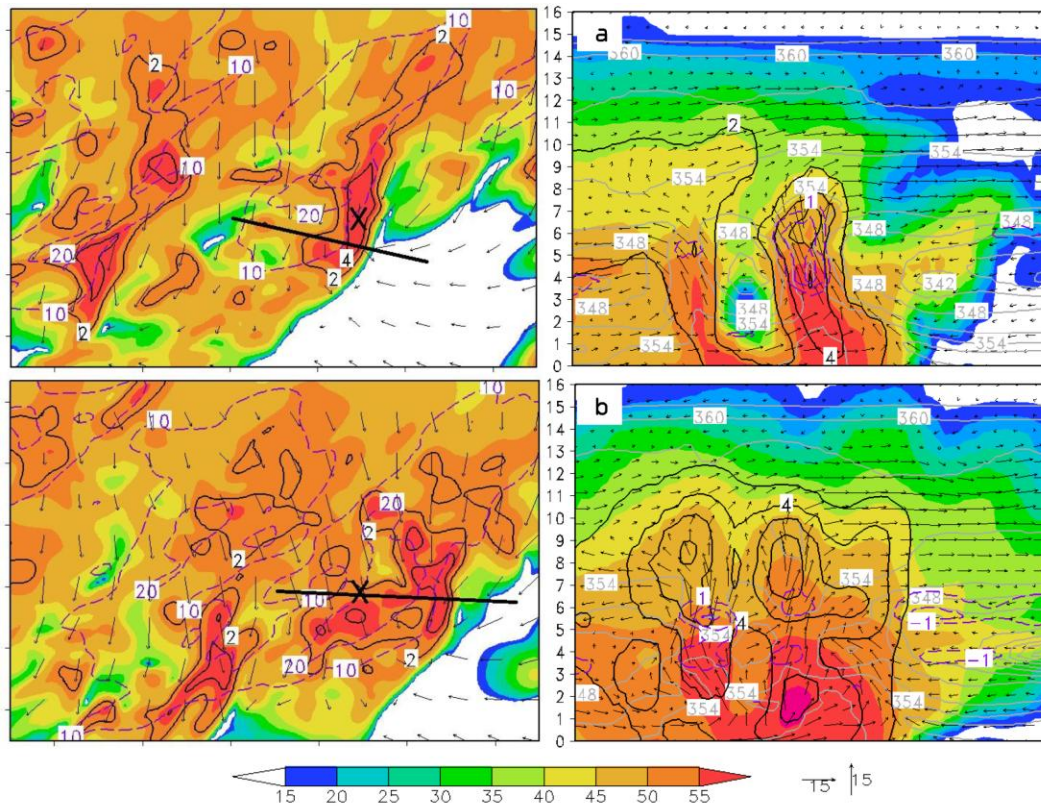


**Figure 11:** Normal cross-sections of simulated reflectivity (dBZ shaded), cloud hydrometeors ( $2.0 \text{ g kg}^{-1}$  intervals),  $\Theta_e$  (3 K grey contour intervals), and temperature perturbations (1 K purple dashed contour intervals), superimposed with in-plane flow vectors at (a) 1720Z and (b) 1740Z. Plan view maps on left indicate cross-section locations, with 'X' denoting the location of Chuzhou.

Although these convective elements allow the rainband to output plenty of rainfall at Chuzhou during this period, this rainband continues to strengthen as it propagates eastward past Chuzhou, influencing precipitation totals downstream. This further strengthening is evident directly after Chuzhou passage in Fig. 11b, at 1740 UTC. A deep cold pool now slightly pulls the updraft upstream, and hydrometeor loading is more evident with values greater than 8 g/kg in the mid to upper levels of the convective cell. The greater hydrometeor concentrations also account for the spike in reflectivity at over 50 dBZ near the surface as precipitation output has gotten stronger.

Even though these features indicate a slight strengthening within 20 minutes of Chuzhou passage, the most noticeable difference in the development of this rainband can be hours later into its evolution, at 2000 UTC in Fig. 13. Using the locations indicated on the simulated reflectivity map of Fig. 12, each cross-section is taken through an embedded convective cell along this now well-developed squall line.

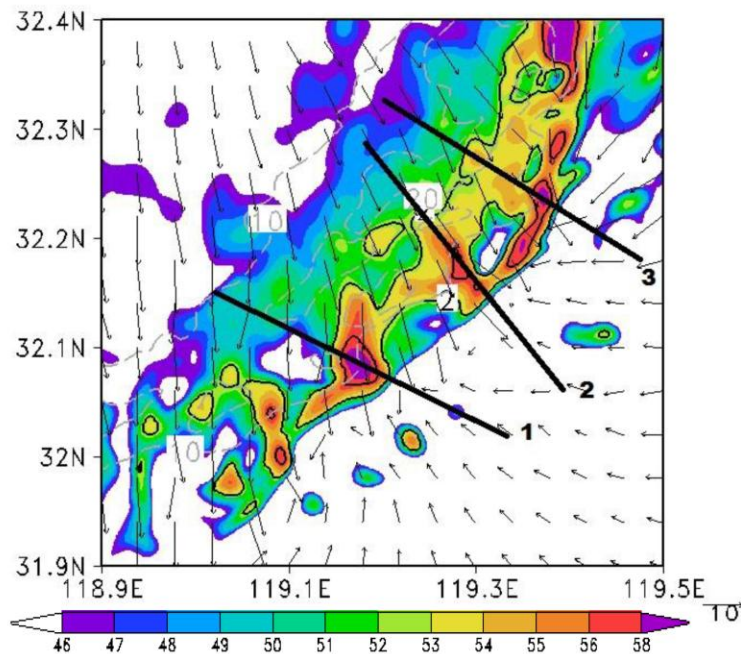


**Figure 12:** Simulated reflectivity (dBZ shaded), cloud hydrometeors ( $2.0 \text{ g kg}^{-1}$  black contour intervals), and 20 minute rainfall (10 mm grey dashed contour intervals) at 20-h simulation. Heavy black lines indicate locations of cross-sections for Figure 13.

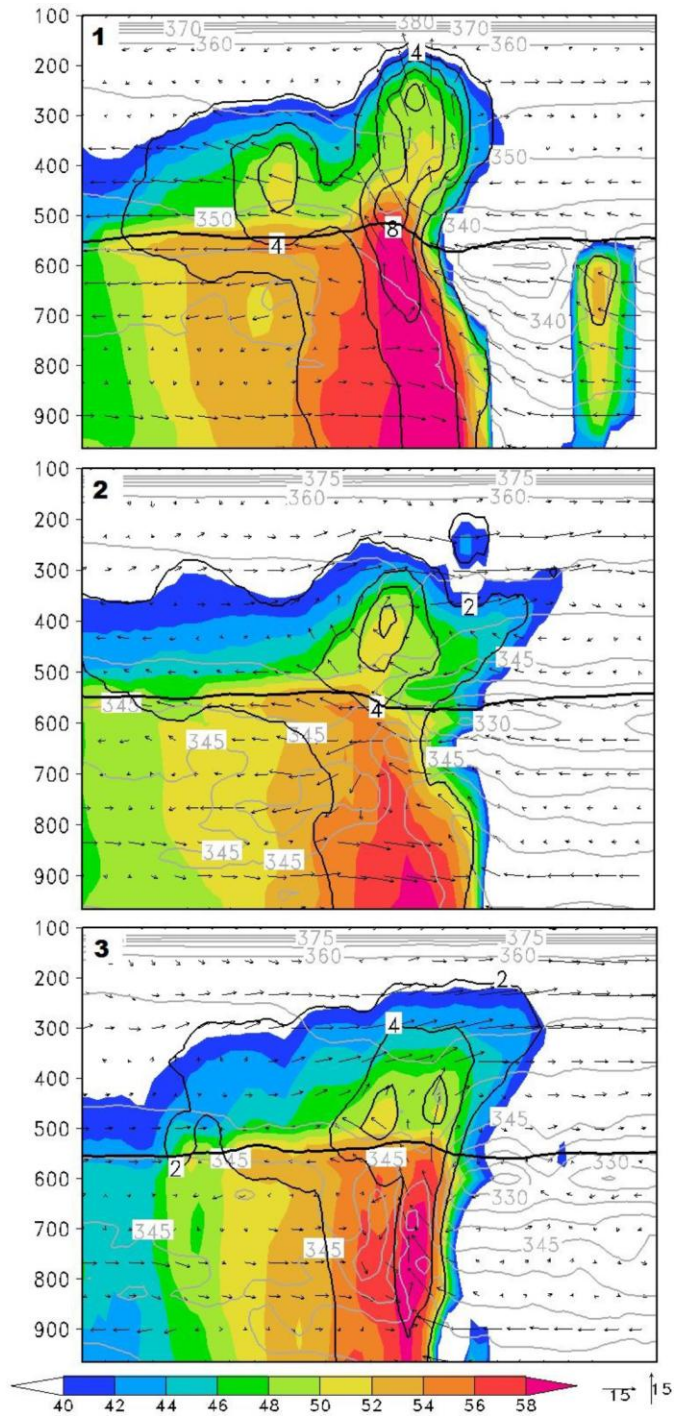


**Figure 13:** Normal cross-sections of simulated reflectivity (dBZ shaded), cloud hydrometeors ( $2.0 \text{ g kg}^{-1}$  black contour intervals), and  $\Theta_e$  (3 K grey contour intervals), superimposed with in-plane flow vectors at 20-h simulation. Thick black line represents freezing level ( $0^\circ\text{C}$ ).

In all three cross-sections, given the minimum shaded reflectivity value of 40 dBZ, it is apparent that the convective line has considerably strengthened with 58+ dBZ values extending vertically through the convective boundary in cross-sections 1 and 3. The prototypical anvil shape indicative of vertically developed, mature convective storms appears in each cross-section, with the updraft in cross-section 1 strong enough to penetrate up to the tropopause. Cloud hydrometeors are also maximized right along this convective edge, with the highest hydrometeor concentrations of 8-10 g/kg above the freezing level, indicating significant ice buildup and potential hail formation as hydrometeors fluctuate vertically above and below the freezing regions of the cumulonimbus cloud. The cold pool is noticeably strong in cross-sections 1 and 2, where the outflow induced circulation works to pull the updraft upstream. In terms of the thermodynamic flows, all three cross-sections show moist, high  $\Theta_e$  air flowing into the convective line from the surface, with dry, low  $\Theta_e$  air still injecting itself into the convective line at midlevels, maximizing both the updrafts and downdrafts, respectively.

The results of these cross-sections suggest that the convective band responsible for the bulk of the extreme precipitation at Chuzhou was subsequently responsible for extreme rainfall produced downstream of Chuzhou as well. Characterized by deep, consistent warm, moist inflow from the south, widespread hydrometeor loading throughout the convective band, and a well-defined outflow boundary during the mature stages at and past Chuzhou passage, this leading rainband, in combination with weaker rainbands before and after, helps explain both the high rainfall totals as well as extreme rainfall rates experienced from this overnight MCS.

## Chapter 4. Summary and conclusions

The results shown in this study give us an understanding of the mesoscale rainband developments associated with this Meiyu driven MCS, and help supplement Part 1 in explaining why extreme rainfall was produced over the Chuzhou region. An analysis of the overlying atmospheric conditions help explain the formation and organization of convective rainbands, while the propagation of the rainbands, as well as the evolution of key variable maximums and vertical cell structure, show why the MCS resulted in extreme rainfall totals.

With respect to the larger scale atmospheric conditions governing the convective development of the MCS, a review of the lateral extent of surface instability as well as the depth of the instability and moisture content proved that conditions were ripe for extreme convective development. Near-surface CAPE values of up to 2000 J/kg straddled the leading convective edge of the MCS, evermore significant given that the convective development occurred overnight, when surface instability is typically at a minimum. The skew-T/Log-P diagrams further illustrated the depth of the instability with a deep layer of moderate CAPE extending into the mid-upper levels. These diagrams also indicated significant moisture content, with saturated or nearly saturated air throughout the depth of the troposphere. These conditions prove the atmosphere was ideal for rainband development, as the rising air was able to quickly condense and produce precipitation.

To fully understand how the convective rainband development resulted in extreme rainfall, an analysis of the rainband organization during the formation process is also

critical as it governed the band training process to follow. The low-level shear was shown to be oriented in a general SW-NE direction, thus indicating overturning boundary layer rolls would also organize linearly in a SW-NE fashion, as these rolls align themselves parallel to the directional wind shear. Given the upward and downward vertical motions associated with these roll vortices, it should be expected that the upward terminus would have the opportunity to condense and form clouds and precipitation if the ambient atmosphere contains the proper moisture content. This appears to be the case for the MCS of study, as the nearly saturated atmosphere along the MCS boundary allowed for heavy convective development along the upward branch of the convective rolls. The result of this is visualized in the general SW-NE orientation of the rainbands responsible for extreme precipitation formation.

This resultant orientation and subsequent eastward propagation initialized band training of the convective rainbands, as each rainband added to the high precipitation total for the affected Chuzhou region. These heavily precipitating rainbands all passed through Chuzhou within a matter of hours between 1600-1900 UTC, not only leading to high precipitation totals but also extreme rain rates within the short time frame. Although each individual rainband contributed to the rainfall total, the second rainband to pass – which developed into the leading convective line shortly afterward – was responsible for the bulk of the precipitation received, as it contained the most extreme rain rates compared to the other relevant rainbands.

The strength and superior influence is further validated given the evolution of important variable maximums, all of which occurred within this leading convective rainband. Vertical velocities, convergence, and cloud hydrometeors were maximized and

steadily increased within the rainband over time, and help explain the continued torrential rainfall reported downstream of Chuzhou, as this convective band continued to develop after Chuzhou passage. The importance of these variables, and for extreme rainfall production in general, is further shown in the vertical structure of this convective band.

Cross-sections both along and normal to the convective band illustrated interesting features which help explain the development of heavy rainfall. The along line vertical structures displayed the echo training process within the rainband, as new convective cells were produced at the southern boundary with the environmental inflow, moving more developed cells deeper into the rainband towards the MCS center. Cross sections taken normal to the rainband further displayed the interaction of the inflow with the convective line's outflow, as the outflow grew in strength and depth over time, eventually matching the inflow strength and producing upright updrafts right around the time of Chuzhou passage. Within the vertical structure, the concentration of hydrometeors steadily increased throughout the rainband, assisting in the development of a stronger moisture boundary at the convective edge through the production of negatively buoyant, precipitation downdrafts. Thus, the hydrometeor loading within the rainband helped produce not only extreme rainfall at the surface but also assisted in the development of the outflow boundary. This strengthened convective boundary allowed for more vertical updraft development, further intensifying the rainband.

In conclusion, the development of convective bands within the MCS lead to their linear orientation through convective initiation of boundary layer roll vortices. As the MCS propagated eastward these linear rainbands advanced eastward as well, with each rainband adding to the precipitation total from the previous band, thus providing the

evidence for band training as the process behind extreme rainfall production. In terms of each specific rainband, the most influential appeared to be the rainband which subsequently developed into the leading convective line shortly after Chuzhou passage. Important convective variables were maximized within this rainband, and helped produce the highest rain rates seen at Chuzhou during this period.

This study provided evidence for band training induced extreme-rainfall production for an MCS event through an analysis of mesoscale structures at a sub-kilometer (0.444 km) resolution. Model analysis of rainfall production at this resolution is still in its infancy, as this paper is one of the first to use a sub-kilometer resolution to produce convective features. However, model resolution will continue to improve as computing power becomes stronger overtime. Even though this study provides an adequate representation of the mesoscale features producing extreme rainfall, the modeling of these small-scale features will only advance as model resolutions become smaller and less reliant on convective parameterization. Thus, our understanding of the smallest circulations within MCS convective bands will only improve with future research.

## References

- Aylward, R. P., and J. L. Dyer, 2010: Synoptic environments associated with the training of convective cells. *Wea. Forecasting*, **25**, 446-464.
- Bosart, L. F., and F. Sanders, 1981: The Johnstown flood of July 1977: A long-lived convective system. *J. Atmos. Sci.*, **38**, 1616-1642.
- Chen, G. T.-J., and C. C. Yu, 1988: Study of low-level jet and extremely heavy rainfall over northern Taiwan in the Meiyu season. *Mon. Wea. Rev.*, **116**, 884-891.
- Chen, S.-J., Y.-H. Kuo, W. Wang, Z.-Y. Tao, and B. Cui, 1998: A modeling case study of heavy rainstorms along the Meiyu front. *Mon. Wea. Rev.*, **126**, 2330-2351.
- Ding, Y.-H., 1994: *Monsoon over China*. Kluwer Academic, 419 pp.
- Dudhia, J., 1989: Numerical study of convection observed during the Winter Monsoon Experiment using a mesoscale two-dimensional model, *J. Atmos. Sci.*, **46**, 3077-3107.
- , 1993: A nonhydrostatic version of the Penn State-NCAR mesoscale model: Validation tests and simulation of an Atlantic cyclone and cold front. *Mon. Wea. Rev.*, **121**, 1493-1513.
- French, A. J., and M. D. Parker, 2010: The response of simulated nocturnal convective systems to a developing low-level jet. *J. Atmos. Sci.*, **67**, 3384-3408.
- Grell, G. A., J. Dudhia, and D. R. Stauffer, 1995: A description of the fifth generation Penn State/NCAR mesoscale model (MM5). NCAR Tech Note NCAR/TN-

398+STR, 138 pp. [Available from NCAR Publication Office, P.O. Box 3000, Boulder, CO 80307-3000.]

Houze, R. A Jr., 2004: Mesoscale convective systems. *Rev. Geophys.*, **42**, RG4003, doi: 10.1029/2004RG000150.

——, B. F. Smull, and P. Dodge, 1990: Mesoscale organization of springtime rainstorms in Oklahoma. *Mon. Wea. Rev.*, **118**, 613-654.

Kain, J. S., 2004: The Kain-Fritsch convective parameterization: An update. *J. Appl. Meteor.*, **43**, 170-181.

Kain, J. S., S. J. Weiss, and D. R. Bright, 2008: Some practical considerations regarding horizontal resolution in the first generation of operational convection-allowing NWP. *Wea. Forecasting.*, **23**, 931-952.

Kato, T., 2006: Structure of the band-shaped precipitation system inducing the heavy rainfall observed over northern Kyushu, Japan on 29 June 1999. *J. Meteor. Soc. Japan*, **84**, 129-153.

Lean, H. W., P. A. Clark, M. Dixon, N. M. Roberts, A. Fitch, R. Forbes, and C. Halliwell, 2008: Characteristics of high-resolution versions of the Met Office Unified Model for forecasting convection over the United Kingdom. *Mon. Wea. Rev.*, **136**, 3408-3424.

LeMone, M. A., 1973: The structure and dynamics of horizontal roll vortices in the planetary boundary layer. *J. Atmos. Sci.*, **30**, 1077-1091.

- Liu, H., D.-L. Zhang, and B. Wang, 2010: Impact of horizontal resolution on the regional climate simulations of the Summer 1998 extreme rainfall along the Yangtze-River Basin. *J. Geophys. Res.*, **115**, D12115, doi:10.1029/2009JD012746.
- Luo, Y., Y. Gong, and D.-L. Zhang, 2013: Initiation and Organizational Modes of an Extreme-Rain-Producing Mesoscale Convective System along a Mei-Yu Front in East China. *Mon. Wea. Rev.*, **142**, 203-221.
- Maddox, R. A., C. F. Chappell and L. R. Hoxit, 1979: Synoptic and meso-scale aspects of flash flood events. *Bull. Amer. Meteor. Soc.*, **60**, 115-123.
- , F. Canova, and L. R. Hoxit, 1980: Meteorological characteristics of flash flood events over the western United States. *Mon. Wea. Rev.*, **108**, 1866-1877.
- , F. Canova, and L. R. Hoxit, 1980: Meteorological characteristics of flash flood events over the western United States. *Mon. Wea. Rev.*, **108**, 1866-1877.
- Moeng, C. H., P. P. Sullivan, 1994: Comparison of shear- and buoyancy-driven planetary boundary layer flows. *J. Atmos. Sci.*, **51**, 999-1022.
- Parker, M. D., 2007: Simulated convective lines with parallel stratiform precipitation. Part I: An archetype for convection in along-line shear. *J. Atmos. Sci.*, **64**, 267-288.
- , and R. H. Johnson, 2003: Structures and dynamics of quasi-2D mesoscale convective systems. *J. Atmos. Sci.*, **61**, 545-567.
- , and ———, 2004: Simulated convective lines with leading precipitation. Part I: Governing dynamics. *J. Atmos. Sci.*, **61**, 1637-1655.

- , and ——, 2004: Simulated convective lines with leading precipitation. Part II: Evolution and Maintenance. *J. Atmos. Sci.*, **61**, 1656-1673.
- Qian, J.-H., W.-K. Tao, and K.-M. Lau, 2004: Mechanisms for torrential rain associated with the Meiyu development during SCSMEX 1998. *Mon. Wea. Rev.*, **132**, 3-27.
- Rotunno, R., and J. B. Klemp, 1982: The influence of the shear-induced pressure gradient on thunderstorm motion. *Mon. Wea. Rev.*, **110**, 136-151.
- , J. B. Klemp, and M. L. Weisman, 1988: A theory for strong, long-lived squall lines. *J. Atmos. Sci.*, **45**, 463-485.
- Schumacher, R. S., 2009: Mechanisms for quasi-stationary behavior in simulated heavy-rain-producing convective systems. *J. Atmos. Sci.*, **66**, 1543-1568.
- , and R. H. Johnson, 2005: Organization and environmental properties of extreme-rain-producing mesoscale convective systems. *Mon. Wea. Rev.*, **133**, 961-976.
- , and ——, 2008: Mesoscale processes contributing to extreme rainfall in a midlatitude warm-season flash flood. *Mon. Wea. Rev.*, **2008**, 3964-3986.
- , and ——, 2009: Quasi-stationary, extreme-rain-producing convective systems associated with midlevel cyclonic circulations. *Wea. Forecasting*, **24**, 555-574.
- Schwartz, C. S., J. S. Kain, S. J. Weiss, M. Xue, D. R. Bright, F. Kong, K. W. Thomas, J. J. Levit, and M. C. Coniglio, 2009: Next-day convection-allowing WRF model guidance: A second look at 2-km versus 4-km grid spacing. *Mon. Wea. Rev.*, **137**, 3351-3372.

- Tao, W.-K., and J. Simpson, 1993: The Goddard cumulus ensemble model. Part I: Model description. *Terr. Atmos. Oceanic Sci.*, **4**, 35-72.
- Wang C.-C., G. T.-J. Chen, T. -C. Chen, and K. Tsuboki, 2005: A numerical study on the effects of Taiwan topography on a convective line during the Meiyu season. *Mon. Wea. Rev.*, **133**, 3217-3242.
- Weisman, M. L., and J. B. Klemp, 1982: The dependence of numerically simulated convective storms on vertical wind shear and buoyancy. *Mon. Wea. Rev.*, **110**, 504-520.
- Young, G. S., D. A. Kristovich, M. R. Hjelmfelt, and R. C. Foster, 2002: Rolls, streets, waves, and more: A review of quasi-two-dimensional structures in the atmospheric boundary layer. *Bull. Amer. Meteor. Soc.*, **83**, 997-1002.
- Zhang, D.-L., and R. A. Anthes, 1982: A high-resolution model of the planetary boundary layer – Sensitivity tests and comparisons with SESAME-79 data. *J. Appl. Meteor.*, **21**, 1594-1609.
- , and J. M. Fritsch, 1986: Numerical simulation of the meso- $\beta$  scale structure and evolution of the 1977 Johnstown flood. Part I: Model description and verification. *J. Atmos. Sci.*, **43**, 1913-1943.
- Zhang, M., and D.-L. Zhang, 2012: Sub-Kilometer simulation of a torrential-rain-producing mesoscale convective system in East China. Part I: Model verification and convective organization. *Mon. Wea. Rev.*, **140**, 184-201.